J. Fluid Mech. (2007), *vol.* 572, *pp.* 311–337.
doi:10.1017/S0022112006003442 Printed in the United Kingdom

Wake instability of a fixed spheroidal bubble

By JACQUES MAGNAUDET AND GUILLAUME MOUGIN†

Institut de Mécanique des Fluides de Toulouse, UMR CNRS/INPT/UPS 5502,
Allée Camille Soula, 31400 Toulouse, France

(Received 8 March 2006 and in revised form 18 July 2006)

Direct numerical simulations of the flow past a fixed oblate spheroidal bubble are carried out to determine the range of parameters within which the flow may be unstable, and to gain some insight into the instability mechanism. The bubble aspect ratio χ (i.e. the ratio of the major axis length over the minor axis length) is varied from 2.0 to 2.5 while the Reynolds number (based on the upstream velocity and equivalent bubble diameter) is varied in the range $10^2 \leqslant Re \leqslant 3 \times 10^3$. As vorticity generation at the bubble surface is at the root of the instability, theoretical estimates for the maximum of the surface vorticity and the surface vorticity flux are first derived. It is shown that, for large aspect ratios and high Reynolds numbers, the former evolves as $\chi^{8/3}$ while the latter is proportional to $\chi^{7/2}Re^{-1/2}$. Then it is found numerically that the flow first becomes unstable for $\chi = \chi_c \approx 2.21$. As the surface vorticity becomes independent of Re for large enough Reynolds number, the flow is unstable only within a finite range of Re, this range being an increasing function of $\chi - \chi_c$. An empirical criterion based on the maximum of the vorticity generated at the body surface is built to determine whether the flow is stable or not. It is shown that this criterion also predicts the correct threshold for the wake instability past a rigid sphere, suggesting that the nature of the body surface does not really matter in the instability mechanism. Also the first two bifurcations of the flow are similar in nature to those found in flows past rigid axisymmetric bluff bodies, such as a sphere or a disk. Wake dynamics become more complex at higher Reynolds number, until the $Re^{-1/2}$-dependency of the surface vorticity flux makes the flow recover its steadiness and eventually its axisymmetry. A qualitative analysis of the azimuthal vorticity field in the base flow at the rear of the bubble is finally carried out to make some progress in the understanding of the primary instability. It is suggested that the instability originates in a thin region of the flow where the vorticity gradients have to turn almost at right angle to satisfy two different constraints, one at the bubble surface, the other within the standing eddy.

1. Introduction

Path instability of millimetre-sized bubbles rising in water is a fascinating phenomenon which has been observed for centuries (Prosperetti *et al.* 2003). Many experiments performed in the second half of the twentieth century (see Magnaudet & Eames 2000 for a review) described the geometrical characteristics of the zigzag or helical trajectories followed by these bubbles, as well as the corresponding bubble shape. Experiments performed in hyperclean water (Duineveld 1995) helped specify the threshold beyond which path instability occurs; in these experiments, the critical bubble Reynolds number was found to be approximately 660, a value for which the

† Present address: L'Air Liquide, Centre de Recherche Claude Delorme 78354 Jouy en Josas, France.

bubble aspect ratio is about 1.85. Nevertheless none of these studies could clearly identify the underlying mechanism responsible for the lateral movements of the bubble and propose a rational instability scenario in agreement with observations. This was essentially because too many uncontrolled phenomena, such as contamination by surfactants, shape oscillations and wake effects, act simultaneously in this complex, though elementary, physical system. This led in particular to speculations about the possibility for a purely irrotational instability mechanism to be responsible for the observed behaviours (Hartunian & Sears 1957; Benjamin 1987). Nevertheless, detailed stability analyses (Meiron 1989) and measurements making use of modern image processing (Ellingsen & Risso 2001) showed that this view was incorrect. It is only recently that numerical studies in which all but one of the possible physical ingredients of the problem could be deliberately ignored showed unambiguously that wake instability is the cause of path instability (Mougin & Magnaudet 2002). More precisely, this study established that there is a one-to-one correspondence between the wake structure and the path geometry. In particular, it was observed that, while the wake is obviously axisymmetric when the bubble rises in a straight line, the transition to the zigzag path coincides with the occurrence of two counter-rotating trailing vortices behind the bubble. Another crucial conclusion of this study was that path instability occurs only for spheroidal bubbles with a sufficient oblateness. In particular, bubbles with an oblateness less than 2.2 were found to rise in straight lines whatever their Reynolds number. Our goal is to provide the first step towards a detailed understanding of the mechanisms at work in the wake dynamics of such millimetre-sized rising bubbles by examining in detail the occurrence and nature of the wake instability for a fixed spheroidal bubble. Although this problem may look academic at first glance, it has a double interest. First, it allows us to discuss similarities and differences with the wake instability of axisymmetric rigid bodies, such as the well-documented case of a rigid sphere. In particular, the role of the boundary condition (no-slip *vs*. no-stress) on the nature and threshold of the instability can be analysed in detail. Secondly, by comparison with results obtained with a freely moving bubble, the fixed-bubble case helps us to understand the influence of the translational and rotational degrees of freedom of the body on the wake evolution. For instance, the difference in the wake structure and wake-induced force at a given Reynolds number may be recorded and used to improve low-dimensional models of wake dynamics. To achieve the above programme, we consider the model problem of a spheroidal bubble of arbitrary oblateness set fixed in a uniform stream directed along the symmetry axis of the bubble. The study makes use of direct numerical simulation (DNS) of the fully nonlinear Navier–Stokes equations. This allows us to obtain the saturated state of the physical system whatever the value of the two control parameters of the problem, namely the bubble aspect ratio and the Reynolds number. During the preparation of this paper, we were made aware that a parallel work carried out independently was dealing with the corresponding linear stability problem (Yang & Prosperetti 2007). Although the two studies focus on different aspects of the problem, they nicely complement each other to clarify the instability scenario of the flow past spheroidal bubbles.

2. Problem statement and numerical method

2.1. *Governing equations*

The flow about the bubble is governed by the standard incompressible Navier–Stokes equations

$$\nabla \cdot \boldsymbol{V} = 0, \tag{2.1a}$$

$$\frac{\partial \boldsymbol{V}}{\partial t} + \boldsymbol{V}\cdot\nabla\boldsymbol{V} = -\frac{1}{\rho}\nabla P + \nu\nabla^2\boldsymbol{V}, \tag{2.1b}$$

ρ and ν being the uniform fluid density and kinematic viscosity, respectively. As the bubble is assumed to be non-deformable and filled with a gas of negligible viscosity, the associated boundary conditions at its surface are

$$\boldsymbol{V}\cdot\boldsymbol{n} = 0, \tag{2.2a}$$

$$\boldsymbol{n}\times\left(\nabla\boldsymbol{V} + {}^t\nabla\boldsymbol{V}\right)\cdot\boldsymbol{n} = 0, \tag{2.2b}$$

$\boldsymbol{n}$ being the outer unit normal to the bubble surface and ^{t} denoting the transpose. The flow is uniform far upstream with a velocity $\boldsymbol{V}_\infty$, so that

$$\boldsymbol{V} \to \boldsymbol{V}_\infty \quad \text{for} \quad \|\boldsymbol{x}\| \to \infty, \tag{2.3a}$$

where $\boldsymbol{x}$ is the distance measured from the bubble centre. The problem under consideration depends on two control parameters. From the bubble volume ϑ we may define the equivalent bubble radius R_{eq} such that $R_{eq} = (3\vartheta/4\pi)^{1/3}$ and introduce the flow Reynolds number $Re = 2V_\infty R_{eq}/\nu$ with $V_\infty = \|\boldsymbol{V}_\infty\|$. As we assume the bubble to have an oblate spheroidal shape, the second control parameter is the aspect ratio $\chi = b/a$, where a and b denote the lengths of the minor and major semi-axes, respectively (with $\vartheta = 4/3\pi ab^2$). In what follows these two control parameters are varied independently, whereas for a real bubble there is only one possible value of χ for each Reynolds number (at least in the steady state), once the liquid properties are specified. Hence varying χ arbitrarily independently of Re means that we artificially change the surface tension without modifying the liquid viscosity.

2.2. *Numerical aspects*

The above system is solved with the JADIM code developed in our group. This code makes use of a finite-volume discretization on a staggered grid. Spatial derivatives are approximated with second-order centred schemes. The velocity field is advanced in time using a third-order Runge–Kutta algorithm for nonlinear and source terms, combined with a Crank–Nicolson semi-implicit algorithm for viscous terms. Incompressibility is achieved at the end of each time step by using a projection technique in which a Poisson equation for a pressure correction is solved. Details about this code may be found in several work, especially Calmet & Magnaudet (1997) for most computational aspects and Magnaudet, Rivero & Fabre (1995) and Legendre & Magnaudet (1998) for specific aspects concerned with curvilinear grids.

In the present study, we make use of an orthogonal curvilinear grid whose inner boundary maps the bubble surface while the outer boundary is spherical. This outer boundary is located at a distance $R_{max} = 50R_{eq}$ from the bubble centroid to avoid confinement effects and allow the wake to be captured over a large distance. The upstream condition (2.3*a*) is prescribed on this outer boundary, except on the part of the boundary that crosses the wake. The wake region is arbitrarily defined as a cone with a semi-angle of 60°, whose apex and axis correspond to the bubble centroid and symmetry axis, respectively. On the part of the outer boundary that crosses this cone, we use a specific non-reflecting condition based on a parabolized form of the momentum equations combined with the requirement that the streamwise pressure gradient does not vary in directions parallel to the boundary (Magnaudet *et al.* 1995).

The grid is based on oblate ellipsoidal coordinates (equation (A 1)), which guarantees that the coordinate lines are orthogonal everywhere. We first generate a plane grid within a meridian plane ($\phi = const.$) and then rotate it about the symmetry axis of the bubble. The grid is made of 64 uniformly distributed cells in the azimuthal direction

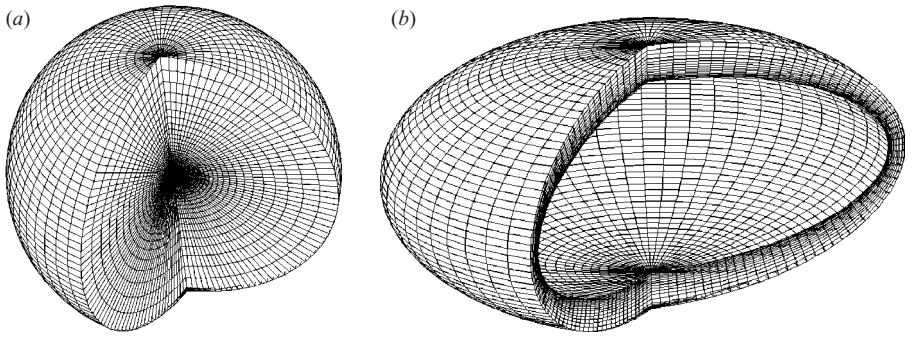

FIGURE 1. Computational grid around an oblate bubble of aspect ratio $\chi = 2.5$. (*a*) General view; (*b*) zoom in the vicinity of the bubble.

(ϕ). In the meridian direction (θ), 65 grid cells are used, with a slight refinement at the rear of the bubble to allow a better description of the wake. Finally, 60 grid cells are distributed in the radial (r) direction. The grid is strongly non-uniform in this direction, since we require that at least five cells lie within the boundary layer for all Reynolds numbers below 2×10^3. As the boundary-layer thickness scales as $Re^{-1/2}R_{eq}$, the above requirement implies that the thickness δ_R of the first row of cells surrounding the bubble must be less than $10^{-2}R_{eq}$. The thickness of the grid cells increases progressively with r, following a geometrical law with a ratio of about 1.12. We checked on several cases that the results to be discussed later are insensitive to a change in either R_{max} or δ_R. Note that the symmetry axis of the grid system introduces a singular behaviour, since on this axis a given point in the physical space (x, y, z) corresponds to different values of ϕ. This singularity results in difficulties in the evaluation of the normal (radial) velocity right on the axis. A specific procedure described by Legendre & Magnaudet (1998) is used to overcome this problem. The techniques used to evaluate the various contributions to the hydrodynamic force experienced by the bubble may be found in the same reference.

An example of the grid used to compute the flow around a bubble with an aspect ratio $\chi = 2.5$ is shown in figure 1.

2.3. *Preliminary tests*

The JADIM code has been extensively used in the past to compute flows in various ranges of Reynolds number past rigid particles and bubbles. Axisymmetric flows past oblate spheroidal bubbles were studied in detail by Blanco & Magnaudet (1995) and we checked that the present version of the code, combined with the grid described above, reproduces closely the corresponding results. Before we start discussing the stability of the flow past a bubble, we briefly show here results obtained at three different Reynolds numbers ($Re = 200$, 250 and 300) in the closely related and well-documented problem of the first stages of the instability of the flow past a fixed rigid sphere.

Figure 2 shows streamlines around the sphere at a Reynolds number $Re = 200$ (here the equivalent radius R_{eq} equals the sphere radius R). The flow is steady and axisymmetric. The length of the recirculation zone is $2.84R$, while the separation angle is $\theta_s = 64.5°$, both quantities being measured from the rear stagnation point. These values are within 2 % of those reported by Tomboulides, Orszag & Karniadakis (1993) and Johnson & Patel (1999). The drag coefficient C_D such that the longitudinal force F_D experienced by the sphere equals $C_D \pi R^2 \rho V_\infty^2/2$ is found to be $C_D = 0.78$,

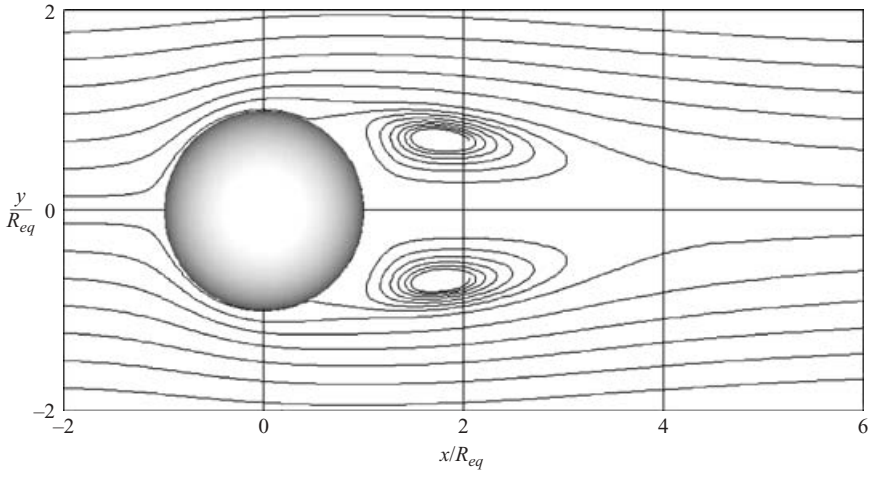

FIGURE 2. Streamlines about a rigid sphere for $Re = 200$.

FIGURE 3. Isosurfaces $\omega_x R/V_\infty = \pm 0.12$ of the streamwise vorticity past a rigid sphere for $Re = 250$.

which also compares well with the value $C_D = 0.79$ reported by the aforementioned authors.

For higher Reynolds numbers, the computation is initialized with the previous stationary solution corresponding to $Re = 200$. A small perturbation with an amplitude $10^{-4} V_\infty$ and a sinusoidal dependency with respect to ϕ is applied during some time steps on the azimuthal velocity over all nodes of a ring of radius $0.3R$ (measured from the symmetry axis) located one radius downstream of the sphere. Figure 3 shows the most salient feature of the fully developed wake structure obtained for $Re = 250$ using the above procedure. The streamwise component of the vorticity which is uniformly zero as long as the flow is axisymmetric is now non-zero, showing that the axial symmetry of the flow has been broken. Indeed, the linear stability analysis of Natarajan & Acrivos (1993) predicts that the flow undergoes a regular bifurcation for $Re \approx 210$, beyond which the first azimuthal mode $m = 1$ is amplified and gives rise to a still stationary but non-axisymmetric flow. The wake topology displayed in figure 3 has long been observed, both experimentally (Magarvey & Bishop 1961; Ormieres & Provansal 1999) and numerically (Tomboulides *et al.* 1993; Johnson & Patel 1999; Ghidersa & Dušek 2000; Tomboulides & Orszag 2000; Thompson, Leweke & Provansal 2001). The pair of streamwise vortices generates a lift component F_L of the force on the sphere (i.e. a component perpendicular to the upstream flow), which can be quantified using a lift

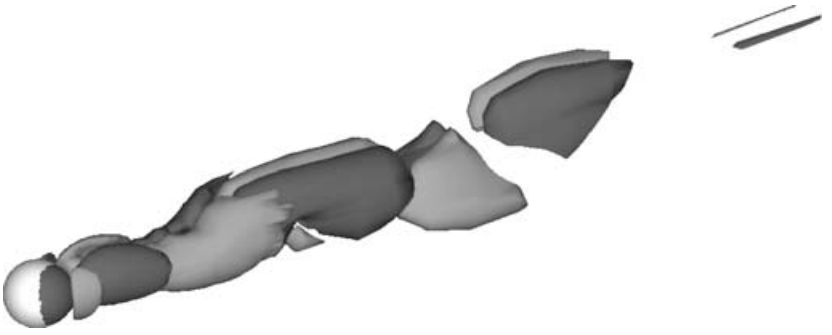

FIGURE 4. Isosurfaces $\omega_x R/V_\infty = \pm 0.12$ of the streamwise vorticity past a rigid sphere for $Re = 300$.

coefficient defined through $F_L = C_L \pi R^2 \rho V_\infty^2/2$. We find $C_L = 0.062$, in perfect agreement with the result reported by Johnson & Patel (1999) for the same Reynolds number.

Figure 4 shows the structure of the same isovalues of the streamwise vorticity for $Re = 300$. The planar symmetry of the flow noticed in the previous regime is preserved, but positive and negative values of ω_x now alternate within each vortex thread. This is a clear indication that the flow is unsteady, the downstream distance along each thread being a direct measure of the time elapsed since the corresponding fluid particle joined the wake. Again this is in agreement with the predictions of the stability analysis of Natarajan & Acrivos (1993) who found that the flow undergoes a Hopf bifurcation for $Re \approx 277$. The aforementioned computational studies in which the fully nonlinear Navier–Stokes equations were considered, indicate a slightly lower threshold, i.e. $Re \approx 272$. The frequency f_0 associated with the shedding process displayed in figure 4 corresponds to a Strouhal number $St = 2 f_0 R/V_\infty$ of 0.133. This value is within 2 to 3 % of those reported by Johnson & Patel (1999) and Tomboulides & Orszag (2000) for the same Reynolds number. The drag and lift coefficients fluctuate about their mean value with the same frequency f_0. In line with results reported by the above authors, the relative fluctuations of C_L are about five time larger than those of C_D ($\approx$10 % instead of 2 %).

3. Vorticity generation on a shear-free bubble

Before we start analysing the numerical results, it is appropriate to discuss some distinctive features of vorticity generation at the surface of a shear-free bubble. As is well known, vorticity is created on curved shear-free surfaces because the vanishing of the tangential stress imposes a specific relation between the tangential velocity and its gradient in the normal direction (Batchelor 1967, p. 366). Let us split the velocity and vorticity at the bubble surface in the form $\boldsymbol{V} = \boldsymbol{V}_S + V_n \boldsymbol{n}$ and $\boldsymbol{\omega} = \boldsymbol{\omega}_S + \omega_n \boldsymbol{n}$, respectively, with $V_n = \boldsymbol{V} \cdot \boldsymbol{n}$ and $\omega_n = \boldsymbol{\omega} \cdot \boldsymbol{n}$. Similarly, we may introduce the surface gradient operator $\nabla_S = \nabla - \boldsymbol{n}\partial/\partial n$, with $\partial/\partial n = (\boldsymbol{n} \cdot \nabla)$. Using the expression of the surface shear stress, it may then be shown that the shear-free condition implies (Wu 1995)

$$\boldsymbol{\omega}_S = 2\boldsymbol{n} \times (\boldsymbol{V}_S \cdot \nabla_S \boldsymbol{n} - \nabla_S V_n), \tag{3.1}$$

where $\nabla_S \boldsymbol{n}$ is the surface curvature tensor. The momentum equation (2.1*b*) may also be projected onto the tangent and normal to the surface to evaluate the vorticity flux that enters the flow and identify the mechanisms that contribute to it (Wu 1995). In

the tangential direction, this yields

$$\nu \frac{\partial \boldsymbol{\omega}_S}{\partial n} = \boldsymbol{n} \times \left(\frac{\mathrm{D}\boldsymbol{V}}{\mathrm{D}t} + \nabla \frac{P}{\rho} \right) + \nu(\nabla_S \omega_n - \boldsymbol{\omega}_S \cdot \nabla_S \boldsymbol{n}), \tag{3.2}$$

where $\mathrm{D}/\mathrm{D}t$ denotes the material derivative. Similarly, the normal projection of the momentum equation, or equivalently the solenoidal condition $\nabla \cdot \boldsymbol{\omega} = 0$, implies that the surface flux of the normal vorticity is

$$\nu \frac{\partial \omega_n}{\partial n} = -\nu(\omega_n \nabla_S \cdot \boldsymbol{n} + \nabla_S \cdot \boldsymbol{\omega}_S), \tag{3.3}$$

where $\nabla_S \cdot \boldsymbol{n}$ is the mean surface curvature. In the situation we are considering, the surface does not deform, which implies $V_n = 0$, so that the last term in (3.1) vanishes. The consequences of this boundary condition were extensively studied by Moore (1963) who showed that it induces a boundary layer whose thickness is $O(R_{eq} Re^{-1/2})$ within which the outer irrotational flow ($\boldsymbol{V}^{Pot}$, P^{Pot}) has to be corrected from a vortical contribution ($\boldsymbol{v}$, p) to satisfy the shear-free condition (2.2*b*). Compared to the case of a no-slip surface, the velocity correction is, however, much weaker because the shear-free condition puts a restriction only on the normal gradient of $\boldsymbol{V}_S$, not on $\boldsymbol{V}_S$ itself. More precisely, Moore showed that within the boundary layer, the meridian and radial components of $\boldsymbol{v}$ are $O(V_\infty Re^{-1/2})$ and $O(V_\infty Re^{-1})$, respectively, whereas the pressure correction p is $O(\rho {V_\infty}^2 Re^{-1})$. These orders of magnitude are useful for evaluating the dominant contributions in (3.1)–(3.3). The first of them indicates that

$$\boldsymbol{\omega}_S = 2\boldsymbol{n} \times \left(\boldsymbol{V}_S^{Pot} \cdot \nabla_S \boldsymbol{n} \right) + O\left((V_\infty / R_{eq}) Re^{-1/2} \right). \tag{3.4}$$

Hence, the leading-order vorticity at the surface is $O(V_\infty / R_{eq})$ and its magnitude may be evaluated directly from the surface curvature and the irrotational velocity $\boldsymbol{V}^{Pot}$. A striking feature of (3.4) is that, in the limit of large Re, the surface vorticity does not evolve with the Reynolds number for a given geometry of the surface. This is at odds with the more familiar situation of a no-slip surface where the magnitude of the surface vorticity increases as $Re^{1/2}$. As we shall see later, this difference has crucial implications on the instability of the flow past a bubble with a prescribed shape.

To simplify (3.2) and (3.3), we first notice that the base flow is axisymmetric, so that the primary vorticity field has only an azimuthal component which does not depend on ϕ. Therefore, ω_n and $\nabla_S \cdot \boldsymbol{\omega}_S$ are both zero and (3.3) merely tells us that the normal vorticity flux is uniformly zero. In (3.2), we first notice that $\mathrm{D}\boldsymbol{V}^{Pot}/\mathrm{D}t$ and $\nabla P^{Pot}/\rho$ balance exactly. Then, expanding the acceleration term so as to make apparent the contribution $\nabla(\boldsymbol{V}^2/2) + \boldsymbol{\omega} \times \boldsymbol{V}$, splitting into tangential and normal components and noting that $\boldsymbol{\omega}_S \times \boldsymbol{V}_S$ is parallel to $\boldsymbol{n}$, it is straightforward to show that in the steady base flow $\mathrm{D}\boldsymbol{v}/\mathrm{D}t$ reduces to $\nabla_S(\boldsymbol{V}_S^{Pot} \cdot \boldsymbol{v}_S + \boldsymbol{v}_S \cdot \boldsymbol{v}_S/2)$, where $\boldsymbol{v}_S$ is the component of $\boldsymbol{v}$ parallel to the surface. Then, using the above estimates for p and $\boldsymbol{\omega}_S$, we are left with

$$\nu \frac{\partial \boldsymbol{\omega}_S}{\partial n} = \boldsymbol{n} \times \nabla_S \left(\boldsymbol{V}_S^{Pot} \cdot \boldsymbol{v}_S \right) + O((V_\infty^2 / R_{eq}) Re^{-1}). \tag{3.5}$$

This equation shows that the leading-order tangential vorticity flux that enters the flow is $O((V_\infty^2/R_{eq})Re^{-1/2})$. It also shows that this flux results from the variation of the 'vortical' kinetic energy $\boldsymbol{V}^{Pot} \cdot \boldsymbol{v}$ along the surface.

Up to this point, the way the magnitude of $\boldsymbol{\omega}_S$ varies with the aspect ratio χ has not been made evident, especially because $\boldsymbol{V}_S^{Pot}$ also depends on the geometry of the surface. To clarify this point, a theoretical determination of the maximum ω_{max} of the surface vorticity is carried out in the Appendix. The main result of this calculation

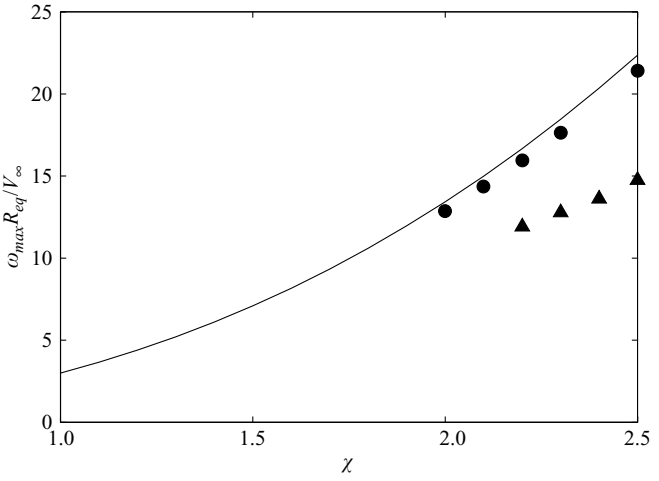

FIGURE 5. Variation of the maximum surface vorticity on an oblate bubble as a function of the aspect ratio χ. —, theoretical prediction, $Re \to \infty$; ●, $Re = 1000$; ▲, $Re = 200$.

is (A 7) which shows that the dimensionless maximum $\omega_{max} R_{eq}/V_\infty$ is equal to 3 for $\chi = 1$ and then increases rapidly with the aspect ratio. This increase results in a dimensionless maximum of about 13.4 for $\chi = 2.0$ and about 22.4 for $\chi = 2.5$, the χ-dependency being proportional to $\chi^{8/3}$ when the oblateness becomes very large.

Figure 5 shows how the above prediction compares with direct numerical predictions of ω_{max} obtained at large but finite Re. For $Re = 200$, viscous effects are still fairly large, so that ω_{max} is significantly lower than predicted from the irrotational solution. In contrast, the numerical results obtained for $Re = 10^3$ are very close to the theoretical prediction and confirm the sharp increase of ω_{max} with the bubble aspect ratio.

The above result can also be used to determine how the tangential vorticity flux (3.5) varies with the bubble aspect ratio in the limit of very large χ. This is achieved by re-writing (3.5) in terms of $\boldsymbol{v}_S$ alone (noting that $\boldsymbol{\omega}_S \approx \boldsymbol{n} \times \partial \boldsymbol{v}_S/\partial n$), using the oblate ellipsoidal coordinate system defined by (A 1) (Moore 1965). Then (A 2) (which shows that ∇_S scales as $\chi^{2/3}/R_{eq}$ at large χ) and (A 4) (which shows that the maximum of $\boldsymbol{V}_S^{Pot}$ scales as χV_∞ in the same limit) imply that, near the bubble equator, the normal derivative $\partial/\partial n$ of vortical quantities scales as $Re^{1/2}\chi^{5/6}/R_{eq}$. Applying this estimate to the asymptotic expression (A 9) of ω_{max} at large χ, leads to the conclusion that the vorticity flux varies as $V_\infty^2/R_{eq}\, O(Re^{-1/2}\chi^{7/2})$ near the equator, as χ and Re tend to infinity. This estimate shows that the vorticity flux also grows very rapidly with the aspect ratio, even though the power 7/2 is probably slightly overestimated in the range of χ which is of primary interest for bubbles rising in low-viscosity liquids (say $\chi < 3.0$). Provided the bubble oblateness is large enough, we can expect that the surface vorticity flux may reach a magnitude comparable to that found at the surface of a rigid sphere in the transitional stage described in § 2.3, as the sharp increase due to the oblateness appears to be able to compensate for the $O(Re^{-1/2})$-dependency for Reynolds numbers of some hundreds.

4. Transition sequence

4.1. *Axisymmetric wake*

Numerical studies considering the axisymmetric Navier–Stokes equations have established that the flow past fixed spheroidal bubbles with a sufficient oblateness may

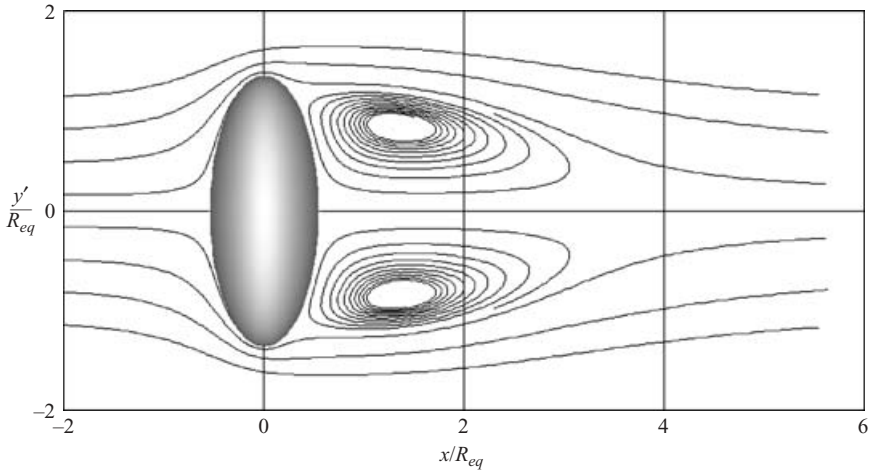

FIGURE 6. Streamlines of the flow past a bubble for $\chi = 2, 5$ and $Re = 100$.

exhibit a standing eddy. This was first pointed out by Ryskin & Leal (1984) who considered axisymmetric deformable bubbles at moderate Reynolds number ($Re <$ 200). Dandy & Leal (1986) and later Blanco & Magnaudet (1995) carried out specific studies with oblate spheroidal bubbles to determine how the size of the standing eddy varies with the bubble aspect ratio and flow Reynolds number. The latter authors showed that only bubbles with an aspect ratio larger than 1.65 exhibit such a wake structure, which, according to the above discussion, suggests that the occurrence of the standing eddy requires a certain amount of vorticity to be injected in the flow from the bubble surface. For a given bubble geometry, these studies showed that the standing eddy occurs beyond a critical Reynolds number $Re_1(\chi)$ and then grows up to a maximum size reached for a Reynolds number $Re = Re_M(\chi)$. Beyond this value, the size of the standing eddy decreases when Re increases and the eddy eventually disappears for a Reynolds number $Re_2(\chi)$. This unusual feature proceeds directly from (3.5) which shows that the amount of vorticity that enters the flow evolves as $Re^{-1/2}$, whereas this amount is independent of Re at large Reynolds number on a no-slip surface because $\boldsymbol{v}_S$ is then $O(V_\infty)$. Bearing in mind that the transport terms in the vorticity equation result in streamwise fluxes that are $O(V_\infty^2/R_{eq})$, i.e. they do not vary with Re, it is clear that for large enough Re and for a given bubble shape, the $O(Re^{-1/2})$ vorticity flux generated at the bubble surface is easily evacuated downstream by the main flow. Hence, vorticity may accumulate behind the bubble and form a standing eddy only in a finite range of Re. The formation of a standing eddy past a shear-free bubble thus appears to be a finite-Re feature driven by the competition between the production of vorticity at the surface and its evacuation in the wake. A nice discussion on this mechanism and the differences with boundary-layer separation in the limit of infinite Reynolds number was given by Leal (1989).

An example of the flow structure in the finite-Re regime where a standing eddy exists is provided by figure 6 corresponding to $\chi = 2.5$ and $Re = 100$. The length of the standing eddy is about $3.0\,R_{eq}$. Note that this picture results from a fully three-dimensional computation, which shows that the axisymmetric flow is stable for this set of parameters.

4.2. *The unstable (χ, Re) range*

In order to determine whether the axisymmetric flow past an oblate bubble is unstable or not, we carried out a series of three-dimensional computations covering the range

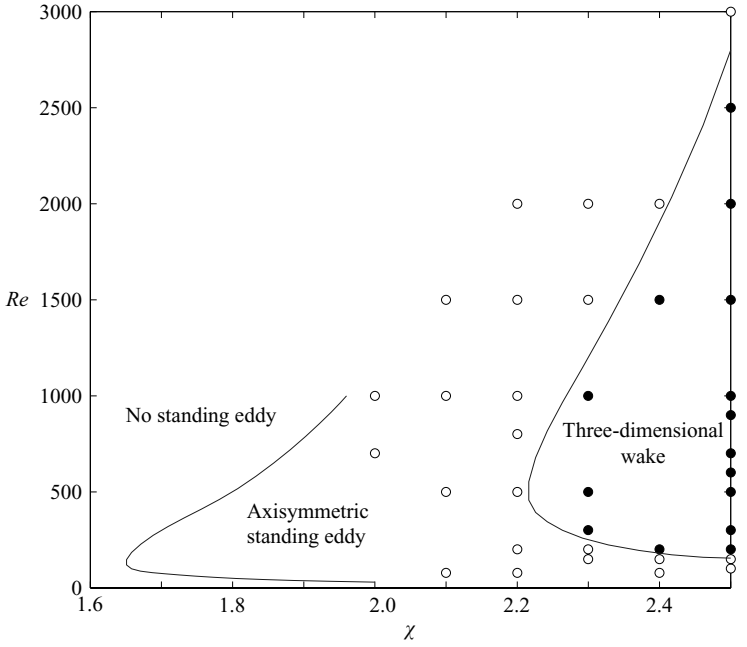

FIGURE 7. Phase diagram showing the parameter range within which the axisymmetric flow is unstable. The curve on the left-hand side corresponds to the limit of the subdomain where Blanco & Magnaudet (1995) detected a standing eddy. ●, unstable; ○, stable.

$Re \in [0, 3000]$ and $\chi \in [2.0, 2.5]$. The computational protocol was similar to that described in § 2.3. In particular, the same azimuthal velocity disturbance was applied during the first time steps of each computation. The flow was said to be stable if the L^2-norm of the azimuthal velocity was found to converge toward zero everywhere in the computational domain. A grid was first generated for each χ, with χ varied with a step of 0.1. Then the Reynolds number was varied within the range of interest for each value of χ. The results of this series of computations are summarized in figure 7 in which the approximate critical curve on the right-hand side was obtained as follows. When the flow was found to be stable at a certain Re and unstable at the next Re (or *vice versa*), a linear interpolation of the corresponding negative and positive growth rates of the volume-averaged energy of the azimuthal motion in the wake was used to determine the corresponding critical Reynolds number, $Re_c(\chi)$. In some cases, we considered a fixed Reynolds number and determined the critical aspect ratio $\chi_c(Re)$ using a similar procedure. Figure 7 reveals that the axisymmetric flow is stable whatever the Reynolds number, as long as the aspect ratio is smaller than a critical value χ_{cm} about 2.21 for which the flow is found to be marginally stable for $Re = 500$. This means in particular that, even though we did not explore aspect ratios close to unity, there is no doubt that the flow past a spherical bubble is stable even for $Re \to \infty$. It is worth noting that the above value of χ_{cm} coincides with that beyond which Mougin & Magnaudet (2002) detected path instability of a freely moving bubble (more precisely, they found the corresponding threshold to lie within the range [2.2, 2.25]). This is, of course, not a coincidence, since Mougin & Magnaudet showed that wake instability is the cause of path instability. Beyond $\chi = \chi_{cm}$, the wake is observed to be unstable within a finite range of Reynolds number whose span increases rapidly with the difference $\chi - \chi_{cm}$. This trend is in line with the discussion in

§ 3 and confirms that, provided the aspect ratio is large enough, the amount of vorticity brought into the flow by the shear-free condition is sufficient for the axisymmetric flow to become unstable. The lower branch of the critical curve corresponds to the value $Re = Re_{min}(\chi)$ below which viscous effects become large enough to limit the magnitude of the vorticity at the bubble surface and maintain the overall stability of the flow. In contrast, the upper branch $Re = Re_{max}(\chi)$ corresponds to the Reynolds number beyond which the $Re^{-1/2}$-dependency of the vorticity flux makes it small enough for the flow to recover its stability, even though the surface vorticity itself does not vary any more with Re in this range. The limit curve corresponding to the domain of existence of a standing eddy in the axisymmetric configuration (as determined by Blanco & Magnaudet 1995) is also reported in figure 7. While the two limit curves have qualitatively similar shapes, it is clear that the latter corresponds to much smaller levels of the surface vorticity and surface vorticity flux. In other words, what our results show is that the subdomain of the (χ, Re)-plane within which the flow past the bubble becomes unstable is included within the one in which a standing eddy exists in the base axisymmetric flow.

The two branches $Re = Re_{min}(\chi)$ and $Re = Re_{max}(\chi)$ of the critical curve obviously correspond to the location where the real part of the most unstable eigenvalue σ (the complex growth rate being defined as $e^{\sigma t}$) of the linear stability problem associated with (2.1)–(2.3) changes sign. We do not attempt to consider this linearized problem here, in contrast to the recent investigation by Yang & Prosperetti (2007). However, a complementary and physically fruitful point of view may be to re-interpret these critical curves by examining, for instance, the way the maximum surface vorticity ω_{max}, defined in the previous section, varies along them. We recorded the corresponding values of $\omega_c(Re) = \omega_{max}(Re, \chi)$ for both $Re = Re_{max}(\chi)$ and $Re = Re_{min}(\chi)$, and fitted them linearly with respect to Re. The simple empirical law that results is

$$\omega_c(Re) R_{eq} / V_\infty \approx 12.5 + 4.3 \times 10^{-3} Re. \tag{4.1}$$

A noticeable point is that this single expression describes accurately both branches of the critical curve. The result (4.1) can be used as an empirical criterion to detect whether the flow corresponding to a given set (χ, Re) is stable or not. That is, knowing the maximum surface vorticity $\omega_{max}(Re, \chi)$ at the Reynolds number under consideration, the flow is unstable (resp. stable) if $\omega_{max}(Re, \chi)$ is larger (resp. smaller) than $\omega_c(Re)$. In particular, it is clear that since ω_{max} does not increase with Re at very large Re for a given χ, the above criterion reproduces the existence of an upper critical Reynolds number $Re = Re_{max}(\chi)$ whose value increases with χ. Similarly, as the Re-prefactor in (4.1) is small, the critical vorticity experiences little variation when the Reynolds number is only a few hundred. As $\omega_{max}(Re, \chi)$ is an increasing function of χ (even though viscosity still limits the value of the surface vorticity in this range), the larger the aspect ratio, the smaller the Reynolds number required for $\omega_{max}(Re, \chi)$ to reach the nearly constant value of $\omega_c(Re)$. This corresponds to the behaviour displayed by the lower branch of the critical curve, where we see that the critical Reynolds number Re_{min} is a decreasing function of χ.

Let us now return briefly to the rigid sphere case. If we try to make use of (4.1) to evaluate the critical maximum vorticity at $Re = 210$ which is approximately the Reynolds number at which the first bifurcation occurs (Natarajan & Acrivos 1993), we find $\omega_c(Re = 210) = 13.4$. Noting that the maximum of the surface vorticity in the axisymmetric situation of figure 2 ($Re = 200$) is 13.1 whereas it is about 16.0 for $Re = 300$ if the flow is constrained to axisymmetry (Magnaudet *et al.* 1995), a linear interpolation suggests that $\omega_{max}(Re = 210)$ is very close to 13.4. Hence, we see that

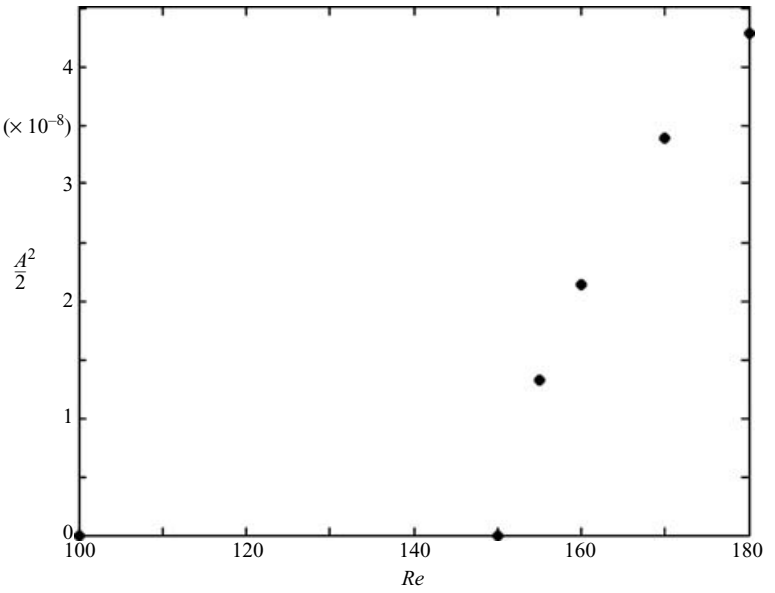

FIGURE 8. Mean energy of the azimuthal motion in the saturated stage ($\chi = 2.5$).

$Re = 210$ is a solution of the equation $\omega_{max}(Re) = \omega_c(Re)$ for a rigid sphere. It thus turns out that the criterion we established on the basis of numerical results obtained with oblate bubbles also predicts accurately the value of the critical Reynolds number at which the first instability of the flow past a rigid sphere occurs. What this successful prediction suggests is that the boundary condition at the body surface (no-slip *vs.* shear-free) is not important *per se* in the generation of the wake instability. What appears to be crucial in this respect is the amount of vorticity produced at the body surface and then injected in the flow. The two different boundary conditions produce different amounts of vorticity and this is why the two sets of critical parameters ($Re = 210$ for the rigid sphere, $Re = Re_{min}(\chi)$ and $Re = Re_{max}(\chi)$ for $\chi > 2.21$ for a shear-free bubble) are different. However, recasting the problem in terms of critical vorticity seems capable of providing a unified view of the behaviour of the two types of axisymmetric bodies in the range of transitional Reynolds numbers.

4.3. *Axial symmetry breaking*

In what follows we focus on the particular bubble geometry corresponding to $\chi = 2.5$ because it offers a broad range of unstable Reynolds numbers. For this particular geometry, the phase diagram of figure 7 indicates that the wake first becomes unstable for $Re_{min} \approx 150$. We computed the flow evolution for several Reynolds numbers in the range $Re \in [150, 190]$, starting from the fully developed results at $Re = 150$ which is actually still a stable configuration. After the instability has saturated, all the resulting flows were found to be stationary, which indicates that the bifurcation is regular, as for a rigid sphere. To characterize this bifurcation better, we recorded the energy of the azimuthal velocity component throughout the wake in the saturated stage. After averaging in space, this allowed us to evaluate the corresponding kinetic energy $(AV_\infty)^2/2$ of the azimuthal motion as a function of Re (Thompson *et al.* 2001). The corresponding results are displayed in figure 8. They clearly show that the bifurcation is supercritical.

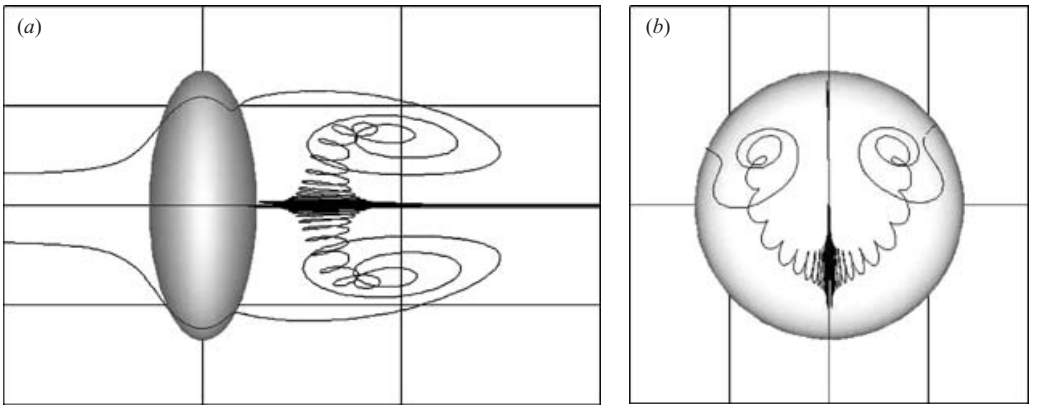

FIGURE 9. Particle paths for $\chi = 2.5$ and $Re = 180$. (*a*) Top view (the y'-axis is perpendicular to the figure; (*b*) back view (the x-axis is perpendicular to the figure).

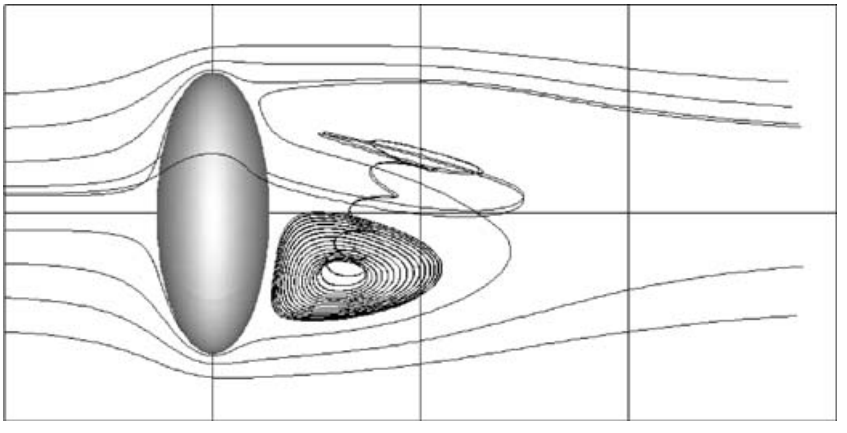

FIGURE 10. Particle paths for $\chi = 2.5$ and $Re = 180$ (side view: the z'-axis is perpendicular to the figure). Note the two paths seen in figure 9 that start in planes parallel to the symmetry plane, go around the bubble, and are eventually captured in the symmetry plane $z' = 0$.

Figures 9 and 10 show some particle paths in the final flow past the bubble for $Re = 180$. As suggested by figure 9, the flow exhibits a symmetry with respect to an (x, y')-plane (also defined as $z' = 0$) whose orientation is dictated by the initial disturbance we impose on the flow. Figure 10 shows that the attached eddy is not axisymmetric any more and is now confined to the lower half of the flow. Fluid particles initially deviated around the eddy, succeed in escaping toward the upper region where they are eventually advected downstream in the wake (particles captured within the eddy follow the same evolution, but the trajectories in figure 10 were stopped before this happens). Two opposite isovalues of the streamwise vorticity component are plotted in figure 11. The corresponding structure made of two counter-rotating threads is similar to that observed in figure 3 for a rigid sphere.

Figure 12 shows the time evolution of the drag and lift coefficients, whose definition was given in § 2. We first notice that after the instability saturates, both coefficients do not vary in time any more, which confirms that the bifurcated flow is stationary. The drag coefficient is found to increase by about 2.5 % after the bifurcation. During the same time, a transverse or lift force (which is directed towards negative y' in the

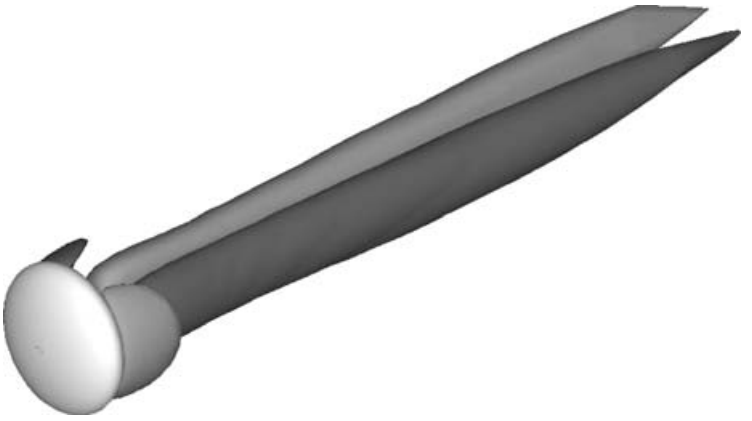

FIGURE 11. Isosurfaces $\omega_x R_{eq}/V_\infty = \pm 0.12$ of the streamwise vorticity ($\chi = 2.5$, $Re = 180$).

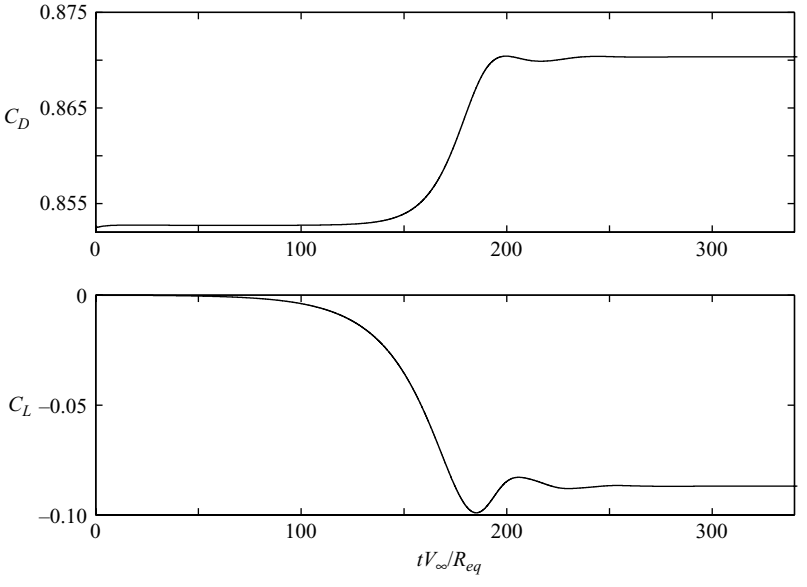

FIGURE 12. Drag and lift coefficients as a function of time ($\chi = 2.5$, $Re = 180$).

present case, owing to the sign of the streamwise vortices) sets in. In the saturated stage, this lift component is about 10 % of the drag force. These ratios are close to those found for $Re = 250$ in the case of a rigid sphere. In figure 12, we can see that the growth of the lift force starts well before (typically 50 advective times before) that of the drag force. This illustrates that the lift component results directly from the linear interaction of the upstream flow with the counter-rotating vortices, whereas the drag increase results from nonlinear interactions which become significant only in the later stages of the instability. Note that in the case of a freely moving bubble, a wake structure similar to that of figure 11 is observed when the bubble is zigzagging. However, in this case, the strength and sign of the trailing vortices vary periodically in time, making the lift force (which drives the horizontal motion of the bubble) change twice during a period of the zigzag. The difference with the

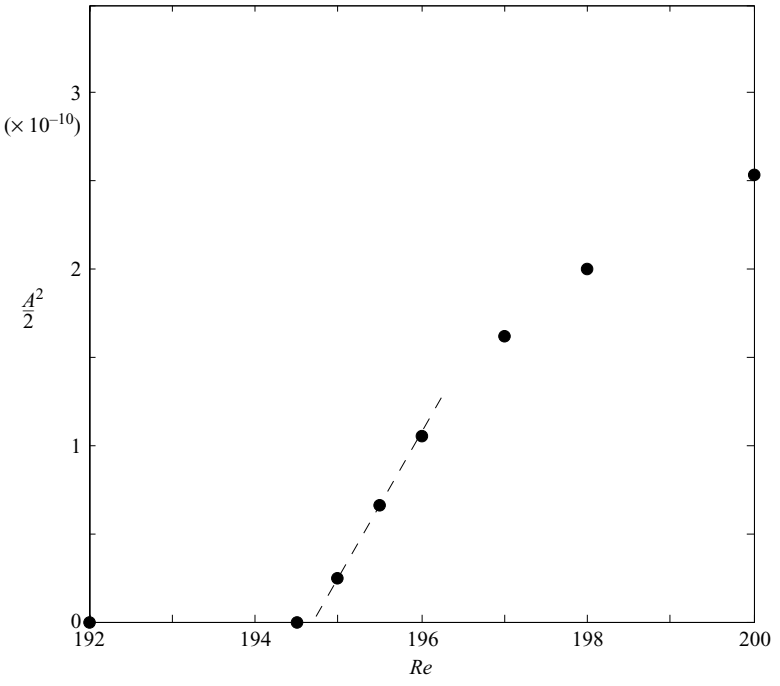

FIGURE 13. Variation of the saturated energy of the time-dependent component of the azimuthal motion ($\chi = 2.5$).

fixed-bubble case is of course due to the feedback effect of the time variations in the bubble velocity and orientation on the wake dynamics.

The results described here and those recently obtained by Yang & Prosperetti (2007) are essentially in agreement. Both studies conclude that the axisymmetric flow past a fixed oblate spheroidal bubble is unstable beyond a certain aspect ratio, and gives birth to a steady non-axisymmetric flow through a regular bifurcation. The critical aspect ratio determined by Yang & Prosperetti (2007) through their linear stability analysis is about 2.1, i.e. slightly lower than that provided by our full nonlinear computations.

4.4. *Transition to unsteadiness*

By further increasing the Reynolds number while keeping χ constant, we found that the flow becomes unsteady for $Re_{cu}(\chi = 2.5) \approx 195$ and then develops a periodic component. We investigated this secondary bifurcation by determining the saturated energy of the time-dependent component of the azimuthal motion using the same approach as for the primary bifurcation. The corresponding result is shown in figure 13. Close to the threshold, the above kinetic energy is seen to grow linearly with $Re - Re_{cu}$, which is characteristic from a supercritical Hopf bifurcation. Also, the Strouhal number evolves according to the law $St = 0.1156 + 4.0 \times 10^{-4}(Re - Re_{cu})$ in the same range of Re. Again, we observe that this second bifurcation has a nature similar to that encountered for a rigid sphere or a disk. Owing to the computer ressources required to determine the above threshold, we did not attempt to obtain the critical curve $Re = Re_{cu}(\chi)$ for the whole range of χ where figure 7 indicates that the axisymmetric wake is unstable. In particular, we did not precisely determine the minimum value of χ (obviously larger than 2.21) for which the secondary bifurcation

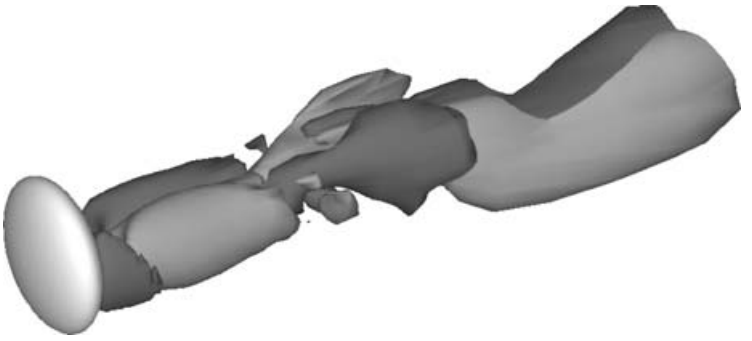

FIGURE 14. Isosurfaces $\omega_x R_{eq}/V_\infty = \pm 0.12$ of the streamwise vorticity ($\chi = 2.5$, $Re = 300$).

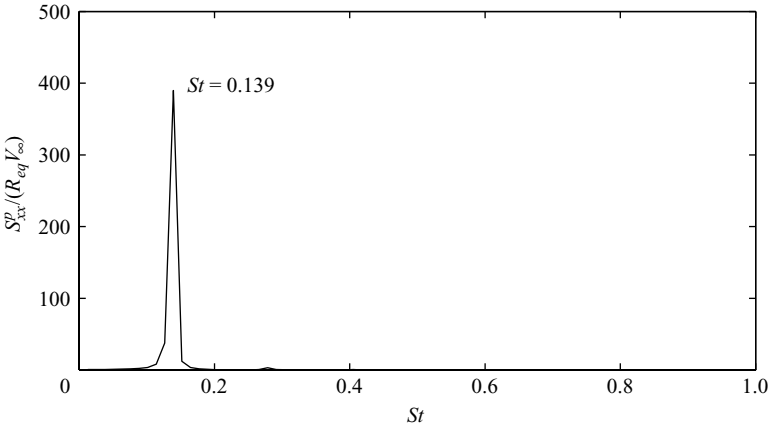

FIGURE 15. Spectrum of the azimuthal velocity fluctuation at $x/R_{eq} = 5.0$, $y/R_{eq} = 0.6$ ($\chi = 2.5$, $Re = 300$).

exists, but the various flow evolutions we obtained suggest that this minimum aspect ratio is in the range $2.3 < \chi < 2.4$. These results are confirmed by Yang & Prosperetti (2007) who also find that unsteadiness occurs in the bubble wake through a Hopf bifurcation which takes place in the range $2.3 < \chi < 2.4$ for $Re = 660$.

Figure 14 shows two opposite isovalues of the streamwise vorticity for $Re = 300$, i.e. far from the threshold determined above. The flow still exhibits a planar symmetry with respect to the plane $z' = 0$, which means that the symmetry plane established by the primary bifurcation is preserved. Unsteadiness is now salient, with an alternation of positive and negative values of ω_x within each thread. An example of the spectral density of the azimuthal velocity fluctuation is given in figure 15. Clearly, only one frequency f_0 is present, even though the distance to the threshold is large in terms of $Re - Re_{cu}$. The corresponding Strouhal number $St = 2 f_0 R_{eq}/V_\infty$ is 0.139, which is in the same range as the value found for the rigid sphere slightly above the corresponding threshold. That only one frequency (i.e. one pair of unstable conjugate complex eigenvalues) exists for $Re - Re_{cu}$ of $O(10^2)$ may seem surprising at first glance. However, as the primary vorticity at the surface of the bubble does not go on growing with the Reynolds number for large Re, $Re - Re_{cu}$ may not be the most appropriate measure of the distance to the threshold. Indeed, if we examine the variation of the maximum of the azimuthal vorticity at the bubble surface from $Re = 195 \approx Re_{cu}$ to

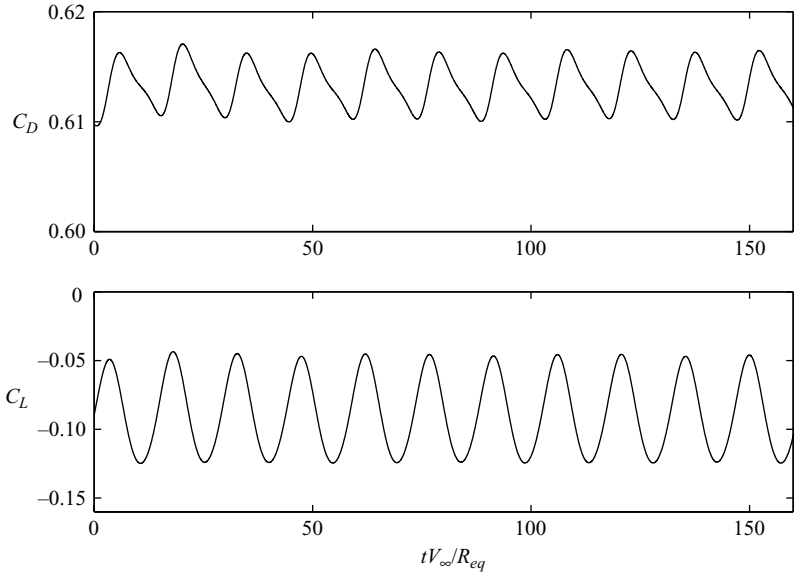

FIGURE 16. Evolution of the drag and lift coefficients ($\chi = 2.5$, $Re = 300$).

$Re = 300$, we find that the two extreme values differ by less than 14 %, whereas the two corresponding Reynolds numbers differ by more than 50 %. Hence, the source of the flow instability is only slightly stronger for $Re = 300$ than for $Re = Re_{cu}$ and no new bifurcation occurs in this range. Figure 16 shows how the drag and lift coefficients evolve after the instability has saturated. The evolution of the lift force is found to be almost sinusoidal, confirming that this force component responds almost linearly to the wake dynamics. In contrast, several harmonics of the fundamental frequency f_0 are present in the drag signal, making it strongly asymmetric. This is a clear indication that these drag oscillations are driven by nonlinear interactions. According to figure 16, the mean lift force is about 14 % of the mean drag force, but the amplitude of the force oscillations is about twelve times larger for the former component than for the latter. Note that the mean lift force is non-zero and keeps the same sign as in the previous flow regime, which indicates that the time-averaged flow is not symmetric with respect to the plane $y' = 0$. This is because, in the immediate vicinity of the bubble surface, the sign of the streamwise vorticity does not vary in time within each thread, a feature already noticed by Johnson & Patel (1999) for a rigid sphere.

4.5. *Further evolution with Re*

Let us now briefly describe the main results of some computational runs we performed in the range $600 \leqslant Re \leqslant 900$ for $\chi = 2.5$. Such Reynolds numbers are typically those for which freely moving bubbles undergo zigzagging and spiralling motion (Duineveld 1995; Mougin & Magnaudet 2002). Isocontours of the streamwise vorticity obtained for $Re = 700$ are displayed in figure 17. This view suggests that the wake still posseses a planar symmetry. To check this aspect better, we recorded the long-time variation of the angle $tg^{-1}(F_{z'}/F_{y'})$ of the lateral force with respect to the fixed (y', z') axes. It turned out that the relative variation of this angle is $O(10^{-7})$, which gives support to the above hypothesis. It is worth noting that in the rigid sphere case, Mittal (1999) found that the planar symmetry is broken between $Re = 350$ and $Re = 375$. That this

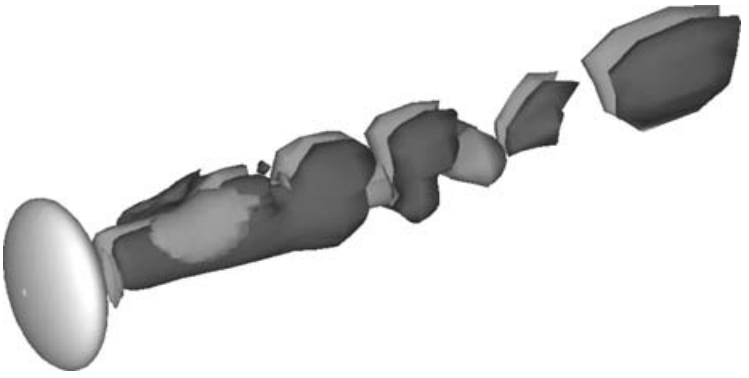

FIGURE 17. Isosurfaces of the streamwise vorticity $\omega_x R_{eq}/V_\infty = \pm 0.12$ ($\chi = 2.5$, $Re = 700$).

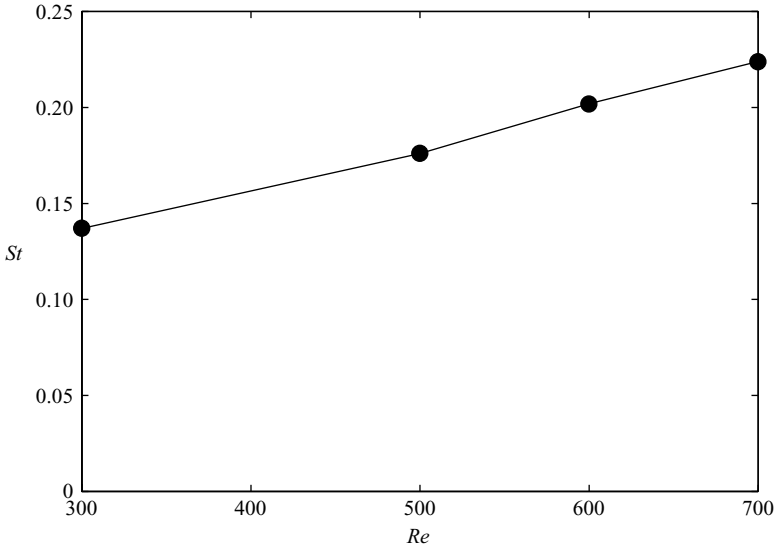

FIGURE 18. Variation of the Strouhal number of the primary shedding mode with the Reynolds number. ($\chi = 2.5$).

symmetry is lost for Reynolds numbers only 30 to 35 % beyond the threshold of the Hopf bifurcation for a rigid sphere while it still subsists for Reynolds numbers more than 3.5 times Re_{cu} for a bubble is remarkable. However, it must be kept in mind that a better indicator of the distance to the threshold in the present case is the maximum of the vorticity at the bubble surface, which varies only by about 35 % from $Re = 195$ to $Re = 700$.

Compared with the previous observations at $Re = 300$, the wavelength of the longitudinal eddies observed at $Re = 700$ is significantly shorter, i.e. the shedding frequency f_0 has increased. This is confirmed by figure 18 which shows that the Strouhal number increases by roughly 60 % from $Re = 300$ to $Re = 700$ and is about 0.22 at the present Reynolds number. Moreover, a secondary mode with a higher Strouhal number ($St = 2 f_1 R_{eq}/V_\infty \approx 0.39$) is now present. Figure 19 indicates that the magnitude of this mode increases with the downstream distance: whereas the signature of the second mode is still weak at $x/R_{eq} = 3.0$, it has become dominant at $x/R_{eq} = 6.0$. Figure 20 shows how the drag and lift coefficients behave in the

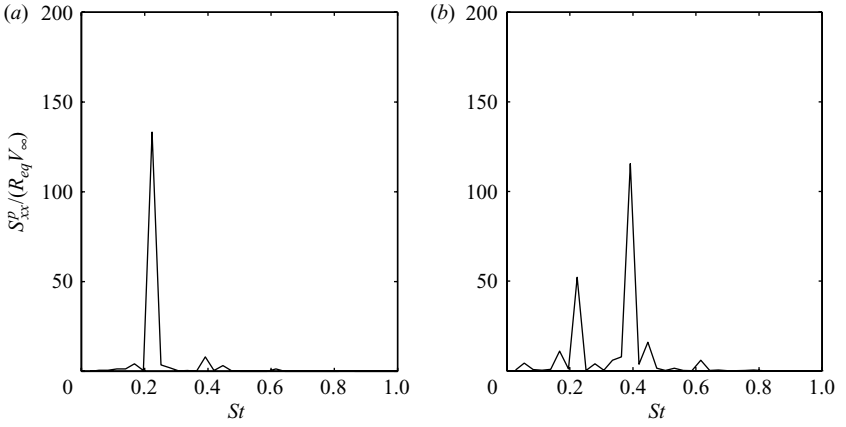

FIGURE 19. Spectra of the azimuthal velocity at: (*a*) $x/R_{eq} = 3.0$, $y/R_{eq} = 0.36$; (*b*) $x/R_{eq} = 6.0$; $y/R_{eq} = 0.4$ ($\chi = 2.5$, $Re = 700$).

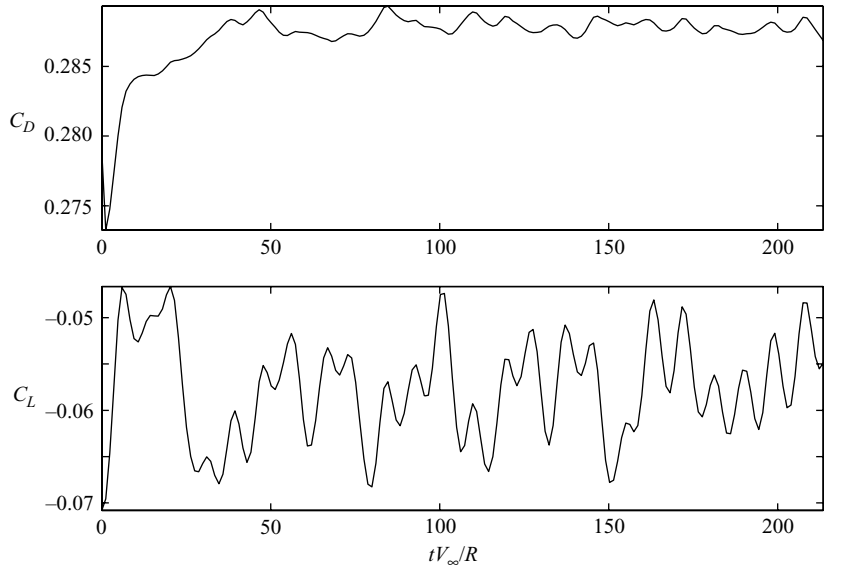

FIGURE 20. Drag and lift coefficients for $\chi = 2.5$, $Re = 700$.

present case. The drag fluctuations have a very small amplitude (about 0.8 % of the mean value), but reflect the joint presence of the two modes. In contrast, the lift fluctuations are still dominated by the primary mode, but also exhibit low-frequency modulations in which the signature of the subharmonic mode $f_0/2$ seems discernible. These fluctuations are large (their crest-to-crest amplitude is about 35 % of the mean force), but the lift force keeps a constant sign with a mean value about 20 % of the mean drag.

As we were mainly interested in the first two bifurcations of the flow, we did not study the properties of the f_1 and $f_0/2$ modes in detail, nor the bifurcations through which they occur. The above results are just given here to indicate that in the above range of Re the complexity of the wake dynamics increases with $Re - Re_{cu}$, a generic feature of transitional wakes. However, in the present situation this complexity cannot

keep on increasing indefinitely, since we know that the wake returns to axisymmetry beyond a certain Reynolds number, which for $\chi = 2.5$ is about 2700. We carried out some extra computations at somewhat higher Reynolds numbers to examine qualitatively the evolution of the wake dynamics. It turned out that a further increase in the Reynolds number up to $Re = 900$ yields a significant decrease in the magnitude of the unsteady component of the wake. In particular, compared to figure 20, the amplitude of lift oscillations is reduced by roughly 25 %. This indicates that the flow is well on the route leading to its return to steadiness. This is not surprising since in this range of Re the maximum vorticity at the bubble surface has almost reached its asymptotic value (see figure 5), so that the $Re^{-1/2}$-decay of the vorticity flux acts efficiently to decrease the amount of vorticity injected in the flow. Since in practice bubbles whose shape is close to an oblate spheroid have rise Reynolds numbers less than 10^3, we did not explore in detail the range $Re \in [10^3, 2 \times 10^3]$ which would have consumed much computational time. Therefore we did not determine the critical Reynolds number Re_{cs} at which the flow recovers its steadiness. While this leaves the picture we obtain for the particular aspect ratio $\chi = 2.5$ slightly incomplete, this overall picture is qualitatively as follows. The flow is steady and axisymmetric for both $Re \leqslant 150$ and $Re \geqslant 2700$, approximately. In between, the flow is steady but non-axisymmetric for $150 < Re < 195$ and $Re_{cs} < Re < 2700$, while it is unsteady only in the intermediate range $195 < Re < Re_{cs}$, with Re_{cs} larger than 10^3 and most probably in the range $[1.5 \times 10^3, 2 \times 10^3]$.

5. Mechanism of the primary instability

Up to this point we have approached physically the process that leads to wake instability through the properties of the surface vorticity and those of the associated flux. Our results show that there is a direct connection between the strength of these quantities and the response of the flow. Nevertheless, it is desirable to obtain a more precise understanding of the mechanism by which, once injected in the base axisymmetric flow, the azimuthal vorticity may lead to its destabilization. The ultimate goal of this quest would be to obtain a rational instability criterion, such as the well-known Rayleigh criterion (Drazin & Reid 1981) for quasi-parallel plane free-shear flows. However, this goal is made very difficult, both by the three-dimensionality of the disturbance to be considered and by the strongly non-parallel character of the near wake. Indeed, little theoretical work has been devoted to the instability of axisymmetric wakes. Most notably, Monkewitz (1988) considered a family of axisymmetric wake profiles and showed that such wakes can be absolutely unstable under certain conditions. However, his analysis considers only quasi-parallel wakes, and the corresponding results, which predict that an $m = 1$ helical mode becomes absolutely unstable beyond a certain Reynolds number, only apply to Reynolds numbers (based on the body characteristic length) of several thousands. Therefore, his results cannot explain the axial symmetry breaking corresponding to the first bifurcation observed in the wake of a bubble or a rigid axisymmetric bluff body. That the non-parallel character of the flow has to be taken into account to elucidate this primary instability mechanism is made clear by examining the spatial structure of the eigenfunction associated with the first unstable mode (see e.g. figures 8 and 9 of Natarajan & Acrivos (1993) for the case of a rigid sphere and a disk). In cylindrical coordinates (σ, ϕ, x), such plots show that the radial and azimuthal velocity components of this eigenmode reach their maximum right on the symmetry axis very close to the rear of the body, whereas the streamwise component reaches its maximum slightly above the axis in the same rear region.

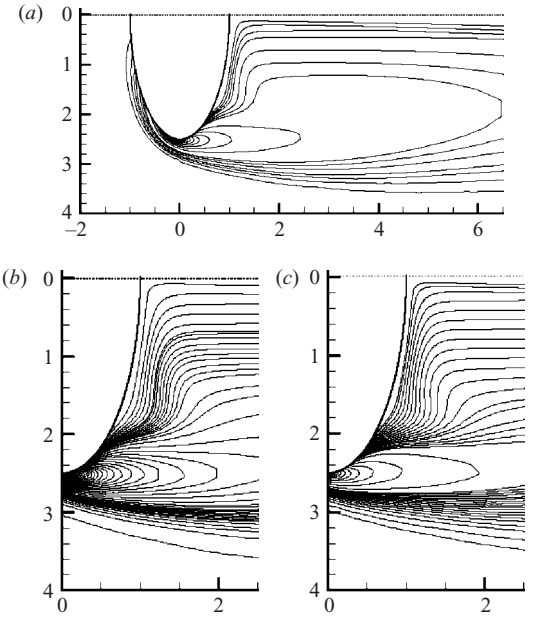

FIGURE 21. Isocontours of the azimuthal vorticity around the bubble in the base flow for $\chi = 2.5$ (the upstream flow is from left to right). (*a*) General view for $Re = 150$. Detailed view in the near-wake region for (*b*) $Re = 150$ and (*c*) $Re = 180$. Vorticity keeps a constant sign on all isocontours displayed in the figure (the vorticity takes tiny values of opposite sign only within a very thin layer at the rear of the bubble, from the separation point to the symmetry axis). The core of the transition region is located in the range $1.2 < x/a < 1.5$, $1.0 < \sigma/a < 1.8$ (the streamwise (horizontal) coordinate x and the radial (vertical) coordinate σ are normalized by the length a of the minor axis of the bubble).

As vorticity is the flow property by which the instability arises, it appears relevant to examine the vorticity distribution in the base flow, close to the threshold. Detail of the isocontours of the azimuthal vorticity just at the back of a bubble with $\chi = 2.5$ are shown in figure 21 for two Reynolds numbers, namely $Re = 150$ which is just below the threshold and $Re = 180$ which is slightly beyond it (since the three-dimensional flow is unstable in the latter case, the corresponding figure was obtained by constraining the flow to remain axisymmetric). Two distinct regions appear in the upper part ($\sigma/a < 2.0$) of the detailed distributions. Very close to the bubble, the isocontours are almost parallel to the bubble surface. The reason for this is that both the surface curvature and the reverse tangential velocity are weak all along this rear part (note that even without the presence of a standing eddy, the surface vorticity is essentially concentrated close to the equator and then decreases very quickly as the distance to the equator increases, as shown by (A 10)). Therefore, in the region under consideration, the bubble surface appears essentially as a vorticity-free boundary; though to a lesser extent, rigid bodies such as a sphere or a disk yield a qualitatively similar conclusion, since the surface shear stress is small in the recirculating region, resulting in a small surface vorticity. On the other hand, somewhat downstream, the ω_ϕ-isocontours are almost parallel to the symmetry axis. This is a direct consequence of the general tendency of ω_ϕ/σ to become closer and closer to a constant within a closed axisymmetric eddy as the Reynolds number increases, a tendency culminating in the Prandtl–Batchelor theorem (Batchelor 1956) in the limit of very large Reynolds

number. Obviously, this theorem does not strictly apply in the present case (i.e. the standing eddy is not close to a Hill vortex) since the Reynolds number is still moderate. However the above tendency is already discernible. It may also be seen in figures 9 and 10 of Fornberg (1988) where the axisymmetric flow past a rigid sphere was computed up to a Reynolds number of 5×10^3.

From the above two arguments, we see that there is a transition region within which the ω_ϕ-isocontours have to turn sharply to satisfy both conditions. According to figure 21, this region takes place approximately in the range $1.2 < x/a < 1.5$, $1.0 < \sigma/a < 1.8$ for $\chi = 2.5$. As can be seen in figure 21, by comparing the shape of the isocontours for the two Reynolds numbers, the angle made within this region by the iso-ω_ϕ with the symmetry axis decreases when the Reynolds number increases because of the stronger and stronger tendency for ω_ϕ/σ to become constant throughout the standing eddy. Clearly, viscous effects cannot be ignored in this matching region, since the nearly zero vorticity condition at the surface originates from viscosity. Within the standing eddy, the maximum velocity is typically $O(\omega_{max} R_{eq})$ (though probably with a small prefactor) when the eddy radius in the σ-direction becomes comparable with that of the body, which is always the case when the flow is close to instability (see figure 6). Therefore, to keep inertial and viscous effects in balance, the thickness of the transition region must evolve as $R_{eq} Re_\omega^{-1/2}$, with $Re_\omega = \omega_{max} R_{eq}^2/\nu$. This transition region, as well as its thinning as the Reynolds number increases is clear in figure 8 of Fornberg (1988). Let us now examine how the various terms of the azimuthal vorticity balance behave in this region. For a steady axisymmetric flow, the vorticity balance reads

$$V_\sigma \frac{\partial \omega_\phi}{\partial \sigma} - V_\sigma \frac{\omega_\phi}{\sigma} + V_x \frac{\partial \omega_\phi}{\partial x} = \nu \left(\frac{\partial}{\partial \sigma} \left(\frac{1}{\sigma} \frac{\partial (\sigma \omega_\phi)}{\partial \sigma} \right) + \frac{\partial^2 \omega_\phi}{\partial x^2} \right) \tag{5.1}$$

In the region under consideration, V_σ (resp. V_x) is positive (resp. negative), owing to the reverse flow, and ω_ϕ has the same sign as ω_{max} within the whole region of interest here. Thus, as long as ω_ϕ keeps on increasing with σ, the first term in the left-hand side of (5.1) is positive and may balance, at least partially, the other two inertial terms which are both negative, since ω_ϕ is increasing with x (see figure 21). In contrast, if $\partial \omega_\phi/\partial \sigma$ vanishes (i.e. the angle θ_ω between the vorticity isocontours and the symmetry axis is 90°), these two terms can only be balanced by the viscous terms, which are indeed both negative according to figure 21. Note, however, that as soon as $\partial \omega_\phi/\partial \sigma = 0$ within a finite range of σ, the first term on the right-hand side reduces to $-\nu \omega_\phi/\sigma^2$, which indicates a Re_ω^{-1}-decrease. The dominant viscous term is then $\nu \partial^2 \omega_\phi/\partial x^2$, implying that in order to maintain the overall balance, the streamwise gradient of ω_ϕ has to become stronger and stronger as Re_ω increases. We believe that such a situation in which the vorticity tends to become discontinuous as $Re_\omega \to \infty$ is intrinsically unstable. The situation is, of course, even worse if θ_ω becomes less than 90°, since all three terms on the left-hand side of (5.1) are then negative.

Based on the above considerations, we strongly suspect that, if the Reynolds number is large enough, the flow within the transition region cannot remain stable if θ_ω becomes less than 90° at some point within it. Figure 21 fully supports this view: θ_ω is slightly more than 90° everywhere for $Re = 150$ and the flow is still stable, while there is a zone of the transition region where this angle is less than 90° for $Re = 180$ and the primary instability has occurred in between. Obviously, our argument has to be confirmed by a detailed stability analysis of the flow in the transition region or of an equivalent flow model. However, such an analysis is beyond the scope of the present work and we just try here to put forward a plausible scenario based

on our numerical observations. If the above argument is correct, then a sufficient condition for the primary instability of the flow at high enough Reynolds number is that $\partial\omega_\phi/\partial\sigma$ vanishes within the interior of the standing eddy. Indeed, similar to what we observed in figure 21, we examined the iso-vorticity distributions for various χ and Re and always detected a region where $\partial\omega_\phi/\partial\sigma$ vanishes when the base flow is very close to the threshold. We also note that in the flow past a rigid sphere, vorticity contours reported by Fornberg (1988) for $Re = 500$ clearly exhibit a part of the transition region where $\partial\omega_\phi/\partial\sigma$ is negative, whereas this quantity almost vanishes in the same zone at $Re = 200$, i.e. close to the threshold, $Re \approx 210$. It is, of course, important to notice that the maximum vorticity at the body surface is involved in the mechanism described, as it enters the eddy Reynolds number Re_ω and therefore governs the thickness of the transition region.

Note that the instability scenario proposed here is specific to axisymmetric flows and of no value in plane wakes past bluff bodies because of their different structure. More precisely, let us assume that the absolute instability that yields the Kármán vortex street in a two-dimensional wake is inhibited by some means, allowing the flow to remain stationary until the Prandtl–Batchelor theorem approximately applies. Then, as the two-dimensional version of this theorem requires the vorticity to be constant within the standing eddy, this constraint does not conflict with the existence of a weak, almost constant, vorticity at the rear part of the body. Therefore, the thin transition region which is central in our argument does not exist in two dimensions. An illustration of this different near-wake structure is provided by the computations performed by Fornberg (1985) past a circular cylinder up to $Re = 600$.

6. Summary and concluding remarks

We carried out direct numerical simulations of the flow past a fixed oblate bubble with a prescribed aspect ratio, the bubble surface being considered as a shear-free boundary. Our results show that, beyond a critical aspect ratio of about 2.21, the flow is unstable within a finite range of Re. This behaviour, which is at odds with that observed for rigid bodies, results from the surface vorticity at a shear-free surface of prescribed shape reaching a finite value when the Reynolds number becomes large. Because of this feature, the vorticity flux injected into the flow evolves as $Re^{-1/2}$, so that the flow recovers its stability for large enough Reynolds number. The reason why the flow may become unstable only if the bubble aspect ratio χ is large enough was clarified by showing that the strength of the vorticity (resp. vorticity flux) at the bubble surface is a strongly increasing function of the aspect ratio, which for large χ behaves as $\chi^{8/3}$ (resp. $\chi^{7/2}$). By varying independently χ and Re, we obtained a quantitative, though approximate, map of the unstable region in the (χ, Re)-plane. In particular, this map shows that the flow past a spherical bubble can never become unstable, whatever the Reynolds number. We showed that the critical curve that limits the unstable region may be re-interpreted in terms of the maximum vorticity at the bubble surface, which yields an empirical criterion to determine whether the flow is stable or not. This criterion was found to work also for a rigid sphere, which suggests that once the amount of vorticity produced at the body surface is known, the nature of this surface, i.e. the boundary condition that takes place on it, is not important by itself. Then we selected a particular aspect ratio, $\chi = 2.5$, to study the flow evolution with the Reynolds number. The flow first undergoes a supercritical regular bifurcation which yields a steady non-axisymmetric flow with, however, a planar symmetry. In this flow configuration, the wake exhibits a pair of counter-rotating threads within which

streamwise vorticity is concentrated. This wake structure, qualitatively similar to that observed behind an airplane, gives rise to a transverse or lift force. Then, by further increasing the Reynolds number, a secondary supercritical Hopf bifurcation occurs. The sign of the streamwise vorticity shed in each thread then changes periodically with a frequency increasing almost linearly with the Reynolds number. The planar symmetry is still maintained in this regime, as well as the sign of the mean lift force. The sequence made of these first two bifurcations is similar to that observed by others for fixed rigid spheres and disks and appears to be typical of axisymmetric bluff bodies, irrespective of their precise shape and of the nature of their surface. Some computations were also carried out at higher Reynolds number and revealed a progressively increasing complexity of wake dynamics which, however, preserves the planar symmetry, at least up to the maximum Reynolds number we explored. Nevertheless, in the same range of Re, the magnitude of unsteady flow characteristics such as drag and lift fluctuations was found to decrease as Re increases, owing to the $Re^{-1/2}$-decay of the surface vorticity flux. This is consistent with the requirement that the flow recovers its steadiness beyond a certain Reynolds number (which we did not determine) and eventually returns to axisymmetry beyond another, larger, Reynolds number.

We finally tried to provide a physical explanation to the mechanism that drives the primary instability. Close to the threshold, examination of the structure of the azimuthal vorticity field in the base flow revealed the existence of a thin layer just behind the bubble where the orientation of the isocontours turn abruptly almost at right angles. Existence of this structure was explained by advocating the constraints the vorticity has to satisfy both at the bubble surface and within the standing eddy. We showed that this layer has a boundary-layer structure, with a thickness scaling as the inverse square root of the maximum surface vorticity. Then, based on the azimuthal vorticity balance, we pointed out that if the vorticity gradient in the direction perpendicular to the symmetry axis vanishes at some point, inertial terms can only be balanced by the streamwise viscous contribution, which certainly leads to an instability beyond a certain Reynolds number. This criterion probably provides only a sufficient condition for the primary wake instability, but appears to be in good agreement with our numerical observations. A detailed stability analysis of the base flow in this region is of course required to confirm the above scenario and obtain a more accurate criterion.

Present results have several potential interests. First, by being concerned with a vorticity production mode different from the usual one at a rigid surface, they help clarify the central role of vorticity, independently of the source that generates it. In other words, what appears to be crucial regarding wake instability is the amount of vorticity the body injects in the flow at a given Reynolds number, not the no-slip or shear-free condition itself. The fact that the sequence of the first two bifurcations is the same for the two classes of bluff bodies and that the empirical criterion we derived from figure 7 also applies to a rigid sphere strongly supports this view. Our results act as a reference for comparing, for a given set of bubble aspect ratio and Reynolds number, the idealized case of a fixed bubble with the more realistic situation of a freely moving bubble. As a first step in this direction, let us mention again that the minimum aspect ratio beyond which we observe wake instability ($\chi_{cm} \approx 2.21$) coincides with the threshold determined by Mougin & Magnaudet (2002) for the onset of path instability. This is an additional indication that wake instability is the cause of path instability of millimetre-sized bubbles rising in low-viscosity liquids. Moreover, the comparison between the two situations may shed light on the role

played by the couplings between the degrees of freedom of the bubble and the dynamics of its wake. In particular, our freely moving bubble computations (Mougin & Magnaudet 2002) show that, once a bubble starts zigzagging and whatever the current Reynolds number, its wake remains as two counter-rotating threads where, at a given time, the streamwise vorticity keeps a constant sign all along each thread. For instance, figure 5 of Mougin & Magnaudet (2002) shows the wake structure of a bubble with an aspect ratio $\chi = 2.5$ zigzagging at a Reynolds number of about 800. In this case, the wake structure is similar to that displayed in figure 11 of the present paper which corresponds to a much lower Reynolds number ($Re = 180$), not to that of figure 17 which corresponds to the much closer value $Re = 700$. Therefore it appears that, owing to the translational and rotational degrees of freedom of the bubble in the freely moving case, the wake never exhibits the alternation of positive and negative vorticity within each thread, characteristic of the wake topology which begins at the Hopf bifurcation. A related aspect is the lift-to-drag ratio, which in the present fixed-bubble case increases progressively with the Reynolds number, but does not exceed 0.20 for $Re = 700$, whereas it is about unity in the same range of Re for the corresponding freely-moving bubble. Exploring the origin of such differences will be the subject of a future paper.

We are extremely grateful to Andrea Prosperetti for providing a preprint of his work with B. Yang and sharing doubts and ideas with us all along the preparation of this paper. This greatly stimulated us in the quest of the instability mechanism. We also thank Richard Adoua for carrying out several extra computations of the base flow and providing figure 21.

Appendix

In this Appendix, we derive the expression of the leading-order vorticity at the surface of an oblate spheroidal bubble. The result is obtained by considering an infinitely large Reynolds number, so that the velocity is given everywhere by the irrotational solution.

Let us first introduce the oblate ellipsoidal coordinate system (ζ, μ, ϕ) such that

$$x = k\zeta\mu, \quad y = k(1+\zeta^2)^{1/2}(1-\mu^2)^{1/2}\cos\phi, \quad z = k(1+\zeta^2)^{1/2}(1-\mu^2)^{1/2}\sin\phi. \tag{A 1}$$

For $\mu \in [-1, 1]$ and $\phi \in [0, 2\pi]$, the surface corresponding to $\zeta = \zeta_0 = (\chi^2 - 1)^{-1/2}$ corresponds to that of an oblate ellipsoid of aspect ratio χ. This ellipsoid has an equivalent radius R_{eq} provided we select $k = R_{eq}(\chi^2 - 1)^{1/2}\chi^{-2/3}$. The metric factors h_μ and h_ζ such that $h_\mu^2 = (\partial x/\partial\mu)^2 + (\partial y/\partial\mu)^2 + (\partial z/\partial\mu)^2$ and $h_\zeta^2 = (\partial x/\partial\zeta)^2 + (\partial y/\partial\zeta)^2 + (\partial z/\partial\zeta)^2$ are given by

$$h_\mu = k\left(\frac{\zeta^2+\mu^2}{1-\mu^2}\right)^{1/2}, \quad h_\zeta = k\left(\frac{\zeta^2+\mu^2}{1+\zeta^2}\right)^{1/2}. \tag{A 2}$$

The translational potential corresponding to a uniform flow of velocity V_∞ parallel to the minor axis of the ellipsoid is (Lamb 1945)

$$\phi_V = kV_\infty\mu\left(\zeta + \frac{1-\zeta\cot^{-1}\zeta}{\cot^{-1}\zeta_0 - \zeta_0\left(1+\zeta_0^2\right)^{-1}}\right). \tag{A 3}$$

The tangential velocity at the surface is then

$$V_\mu(\zeta_0) = V_\infty \left(\frac{1-\mu^2}{\zeta_0^2+\mu^2}\right)^{1/2} \left(\zeta_0 + \frac{1}{\zeta_0 - \left(1+\zeta_0^2\right)\cot^{-1}\zeta_0}\right). \tag{A 4}$$

The surface curvature tensor $\nabla_S \boldsymbol{n}$ may be written in the form $\nabla_S \boldsymbol{n} = H_\mu^n \boldsymbol{e}_\mu \boldsymbol{e}_\mu + H_\phi^n \boldsymbol{e}_\phi \boldsymbol{e}_\phi$, where H_μ^n and H_ϕ^n (resp. $\boldsymbol{e}_\mu$ and $\boldsymbol{e}_\phi$) are the surface radii of curvature (resp. the unit vectors) in the meridian and azimuthal directions, respectively. The radius of curvature H_μ^n at the ellipsoid surface is given by

$$H_\mu^n(\zeta_0) = \frac{1}{h_\mu h_\zeta}\frac{\partial h_\mu}{\partial \zeta}(\zeta_0) = \frac{\zeta_0\left(1+\zeta_0^2\right)^{1/2}}{k\left(\zeta_0^2+\mu^2\right)^{3/2}}. \tag{A 5}$$

According to (A 4) and (A 5), $V_\mu(\zeta_0)$ and $H_\mu^n(\zeta_0)$ both reach their maximum at the equator of the ellipsoid ($\mu = 0$). Therefore, from (3.4) we conclude that the surface vorticity $\boldsymbol{\omega}_S = \omega_\phi \boldsymbol{e}_\phi$ also reaches its maximum at this position, the magnitude of this maximum being

$$\omega_{max} = 2\frac{V_\infty}{k\zeta_0^3}\frac{\left(1+\zeta_0^2\right)^{1/2}}{\left(1+\zeta_0^2\right)\cot^{-1}\zeta_0 - \zeta_0}. \tag{A 6}$$

Replacing ζ_0 and k by their values as a function of χ in (A 6) then yields

$$\omega_{max} = 2\frac{V_\infty}{R_{eq}}\frac{\chi^{5/3}(\chi^2-1)^{3/2}}{\chi^2\sec^{-1}\chi - (\chi^2-1)^{1/2}}. \tag{A 7}$$

When $\chi \to 1$, $\sec^{-1}\chi \to \frac{1}{3}(\chi^2-1)^{1/2}(4-\chi^2)$, so that we recover the well-known result (Moore 1963)

$$\omega_{max}(\chi = 1) = 3\frac{V_\infty}{R_{eq}}. \tag{A 8}$$

At very large χ, $\sec^{-1}\chi \to \pi/2$, so that

$$\omega_{max} \to \frac{4}{\pi}\frac{V_\infty}{R_{eq}}\chi^{8/3}. \tag{A 9}$$

From (A 4) and (A 5) we also find that at any point of the surface, the vorticity is

$$\omega_\phi(\mu) = \omega_{max}\frac{(1-\mu^2)^{1/2}}{(1+(\chi^2-1)\mu^2)^2}. \tag{A 10}$$

This result indicates for instance that at $y = y(\omega_{max})/2$, which according to (A 1) is obtained for $\mu^2 = 3/4$, $\omega_\phi/\omega_{max} = 1/(2(1+3(\chi^2-1)/4)^2)$, which for large χ tends toward $8\chi^{-4}/9$.

REFERENCES

Batchelor, G. K. 1956 On steady laminar flow with closed streamlines at large Reynolds number. *J. Fluid Mech.* **1**, 177–190.

Batchelor, G. K. 1967 *An Introduction to Fluid Dynamics*. Cambridge University Press.

Benjamin, T. B. 1987 Hamiltonian theory for motion of bubbles in an infinite liquid. *J. Fluid Mech.* **181**, 349–379.

Blanco, A. & Magnaudet, J. 1995 The structure of the axisymmetric high-Reynolds number flow around an ellipsoidal bubble of fixed shape. *Phys. Fluids* **7**, 1265–1274.

Calmet, I. & Magnaudet, J. 1997 Large-eddy simulation of high-Schmidt number mass transfer in a turbulent channel flow. *Phys. Fluids* **9**, 438–455.

Dandy, D. S. & Leal, L. G. 1986 Boundary layer separation from a smooth slip surface. *Phys. Fluids* **29**, 1360–1366.

Drazin, P. G. & Reid, W. H. 1981 *Hydrodynamic Stability*. Cambridge University Press.

Duineveld, P. C. 1995 The rise of an ellipsoidal bubble in water at high Reynolds number. *J. Fluid Mech.* **292**, 325–332.

Ellingsen, K. & Risso, F. 2001 On the rise of an ellipsoidal bubble in water: oscillatory paths and liquid-induced velocity. *J. Fluid Mech.* **440**, 235–268.

Fornberg, B. 1985 Steady viscous flow past a circular cylinder up to Reynolds number 600. *J. Comput. Phys.* **61**, 297–320.

Fornberg, B. 1988 Steady viscous flow past a sphere at high Reynolds numbers. *J. Fluid Mech.* **190**, 471–489.

Ghidersa, B. & Dušek, J. 2000 Breaking of axisymmetry and onset of unsteadiness in the wake of a sphere. *J. Fluid Mech.* **423**, 33–69.

Hartunian, R. A. & Sears, W. R. 1957 On the stability of small gas bubbles moving uniformly in various liquids. *J. Fluid Mech.* **3**, 27–47.

Johnson, T. A. & Patel, V. C. 1999 Flow past a sphere up to Reynolds number of 300. *J. Fluid Mech.* **378**, 10–70.

Lamb, H. 1945 *Hydrodynamics*, 6th edn. Dover.

Leal, L. G. 1989 Vorticity transport and wake structure for bluff bodies at finite Reynolds number. *Phys. Fluids* A **1**, 124–131.

Legendre, D. & Magnaudet, J. 1998 The lift force on a spherical bubble in a viscous linear shear flow. *J. Fluid Mech.* **368**, 81–126.

Magarvey, R. H. & Bishop, R. L. 1961 Transition range for three-dimensional wakes. *Can. J. Phys.* **39**, 1418–1422.

Magnaudet, J. & Eames, I. 2000 The motion of high-Reynolds-number bubbles in inhomogeneous flows. *Annu. Rev. Fluid Mech.* **32**, 659–708.

Magnaudet, J., Rivero, M. & Fabre, J. 1995 Accelerated flows past a rigid sphere or a spherical bubble. Part 1. Steady straining flow. *J. Fluid Mech.* **284**, 97–135.

Meiron, D. I. 1989 On the stability of gas bubbles rising in inviscid fluid. *J. Fluid Mech.* **198**, 101–114.

Mittal, R. 1999 Planar symmetry in the unsteady wake of a sphere. *AIAA J.* **37**, 388–390.

Monkewitz, P. A. 1988 A note on vortex shedding from axisymmetric bluff bodies. *J. Fluid Mech.* **192**, 561–575.

Moore, D. W. 1963 The boundary layer on a spherical gas bubble. *J. Fluid Mech.* **16**, 161–176.

Moore, D. W. 1965 The velocity of rise of distorted gas bubbles in a liquid of small viscosity. *J. Fluid Mech.* **23**, 749–766.

Mougin, G. & Magnaudet, J. 2002 Path instability of a rising bubble. *Phys. Rev. Lett.* **88**, 14502.

Natarajan, R. & Acrivos, A. 1993 The instability of the steady flow past spheres and disks. *J. Fluid Mech.* **254**, 323–344.

Ormieres, D. & Provansal, M. 1999 Transition to turbulence in the wake of a sphere. *Phys. Rev. Lett.* **83**, 80–83.

Prosperetti, A., Ohl, C., Tijink, A., Mougin, G. & Magnaudet, J. 2003 Leonardo's paradox. Appendix to A. Prosperetti, C. D. Ohl & A. Tijink, *J. Fluid Mech.* **482**, 286–289.

Ryskin, G. & Leal, L. G. 1984 Numerical solution of free-boundary problems in fluid mechanics. Part 2. Buoyancy-driven motion of a gas bubble through a quiescent liquid. *J. Fluid Mech.* **148**, 19–35.

Thompson, M., Leweke, T. & Provansal, M. 2001 Kinematics and dynamics of sphere wake transition. *J. Fluids Struct.* **15**, 1575–585.

Tomboulides, A. G. & Orszag, S. A. 2000 Numerical investigation of transitional and weak turbulent flow past a sphere. *J. Fluid Mech.* **416**, 45–73.

Tomboulides, A. G., Orszag, S. A. & Karniadakis, G. E. 1993 Direct and large-eddy simulation of axisymetric wakes. *AIAA Paper* 93-0546.

Wu, J. Z. 1995 A theory of three-dimensional interfacial vorticity dynamics. *Phys. Fluids* **7**, 2375–2395.

Yang, B. & Prosperetti, A. 2007 Linear stability of the flow past a spheroidal bubble. *J. Fluid Mech.* (to appear).